Reconstruction of pH-universal atomic Fe—N—C catalysts towards oxygen reduction reaction

Zhe Chen [a], Dengyu Zhao [a], Cong Chen [a], Yuan Xu [a], Congli Sun [c], Kangning Zhao [a], Muhammad Arif Khan [b], Daixin Ye [a,*], Hongbin Zhao [a,*], Jianhui Fang [a], Xueliang Andy Sun [d], Jiujun Zhang [a]

[a] College of Sciences & Institute for Sustainable Energy, Shanghai University, Shanghai 200444, PR China
[b] School of Materials Science and Engineering, Shanghai University, Shanghai 200444, PR China
[c] NRC (Nanostructure Research Centre), Wuhan University of Technology, Wuhan 430070, PR China
[d] University of Western Ontario, London N6A 5B8, Canada

HIGHLIGHTS

- The three-dimensional hierarchically architectural Fe—N—C catalyst was prepared through silicon template.
- The ammonia-assisted secondary pyrolysis boosted the density of Fe—N$_x$ active sites.
- The Fe—N—C catalyst delivers outstanding ORR activity in pH-universal electrolyte.

GRAPHICAL ABSTRACT
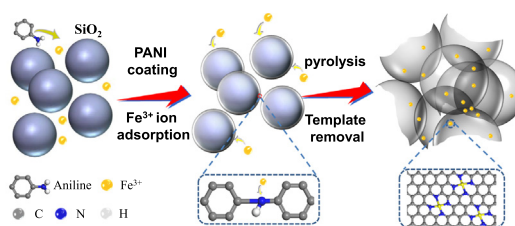
ABSTRACT

Constructing of single atom catalysts that can stably exist in various energy conversion and storage devices is still in its infancy. Herein, a geometrically optimized three-dimensional hierarchically architectural single atomic Fe—N—C catalyst with fast mass transport and electron transfer is rationally developed by post-molecule pyrolysis assisted with silicon template and reconstructs by ammonia treating. The ammonia-assisted secondary pyrolysis not only compensates for the volatilization of nitrogen species contained in organic precursors but also optimizes the surface structure of Fe—N—C catalyst, thus increasing the content of pyridinic nitrogen and boosting the density of active sites (Fe—N$_x$) in Fe—N—C samples. In addition, the pyridinic nitrogen adjusts the electronic distribution in Fe 3d active center and promotes the catalytic performances. Therefore, this hollow spherical atomically dispersed Fe—N—C catalyst delivers outstanding oxygen reduction reaction (ORR) activity in pH-universal electrolyte and surpasses the most reported values.

© 2020 Published by Elsevier Inc.

1. Introduction

The ever-growing energy consumption prompts researchers to constantly address the emerging environmental crisis and develop renewable energy storage and conversion technologies [1–4]. However, the sluggish kinetic of oxygen reduction reaction (ORR) significantly restricted the advancement of new-generation devices such as fuel cells and metal-air batteries. Platinum and its alloys are deemed as the most preferable candidates for ORR, while their preciousness and vulnerability were not considered in large-scale commercial applications [5]. For these reasons, multiplicate state-of-the-art precious-metal-free electrocatalysts including transition-metal macrocyclic compounds [6,7], metal oxides[8], metal sulfides [9], and transition-metal catalysts with M-N$_x$ structure [10–12] as active sites have been excavated. Nevertheless, these electrocatalysts still arduously afford their demands

* Corresponding authors.

E-mail addresses: daixinye@shu.edu.cn (D. Ye), hongbinzhao@shu.edu.cn (H. Zhao).

to replace Pt in pH-universal electrolyte, especially in acid and neutral medium [13].

Nowadays, single atom catalysts (SACs) have become a novel hotspot due to their unique electronic structure and coordination environment [14]. With ultra-highly atomic utilization, outstanding intrinsic activity, clarified catalytic mechanism, and fully exposed active sites, SACs have been widespreadly used in water splitting [15], carbon dioxide reduction reaction (CO_2RR) [16], nitrogen reduction reaction (NRR) [17], ORR [18], and so on. As for ORR, M-N_x is suggested as the main active site owing to the hybridization between the N 2p and M 3d, especially Fe-N_4 with a planar structure[19,20]. Fe-N_4 can significantly perturb the electronic structure of the carbon around it, thereby promoting the ORR reaction [21]. The Fe—N—C catalyst obtained by calcination at a high temperature has a sudden change in the ligand environment around the Fe-N_x active site from an electron-rich ring to an electron-deficient graphite ligand. The electron-absorbing environment of the graphitic carbon will cause the oxygen reduction potential of metal ions to shift to a corrected potential, thereby obtaining a corrected ORR starting potential. Furthermore, the M-N_x structure is similar to phthalocyanine-iron, which makes it highly stable under acidic condition. For example, the Fe—N—C catalysts generated by the pyrolysis of phthalocyanine and Fe precursors can stably exist under acidic conditions and exhibit excellent catalytic activity for oxygen reduction [22]. In addition, other active sites toward ORR also were reported, including graphitic-N, pyrrolic-N, pyridinic N, and even the sp^2 C near oxygen on anthracene and carbon adjacent to carboxyl group [23]. Therefore, the mechanism towards 2e-ORR and 4e-ORR is still not clear and even conflicted.

Considering about non-precious metal catalysts have poor acid stability, their application under acidic conditions face great challenges. At present, only few of Fe—N—C—based catalysts can stably exist in acid fuel cell systems[24,25]. At the same time, regardless of the ORR reaction under acidic or alkaline conditions, there is a possibility of pH change existing dynamically under the micro environment. For instance, the rapid consumption of protonic acid increases local alkalinity under acidic conditions and constant OH^- depletion leads to pH decrease again under alkaline conditions. Therefore, it is of great significance to develop a non-precious metal oxygen reduction catalyst which is stable and highly active at full pH ranges.

Herein, we designed a three-dimensional hierarchically architectural single atomic Fe—N—C catalyst with fast mass transport and electron transfer. The catalyst was developed by post-molecule pyrolysis assisted with silicon template and reconstructed by ammonia treating. The SiO_2 template is conducive to construct larger specific surface area to anchor abundant active sites and the ammonia results in more active and durable catalysts. The atomically dispersed Fe were successfully revealed by aberration-corrected scanning transmission electron microscopy (STEM) and a paramount ORR performance was witnessed by systematic electrochemical charactering. The structural optimized Fe—N—C catalyst delivers outstanding ORR catalytic activity and superior long-time stability in alkaline, acidic, and neutral electrolyte, comparable to that of the commercial Pt/C and most reported single-atom based catalysts.

2. Experimental

2.1. Catalyst synthesis

Preparation of SiO_2 spheres: SiO_2 particles was synthesized according to the as reported Stöber method. Briefly, 2.4 mL TEOS was introduced into the solution which contained with 60 mL absolute ethanol, 2.8 mL ammonia hydroxide and 20 mL deionized

water by dropwise. Then, the SiO_2 template was obtained after stirring, filtrating, washing, and drying.

Preparation of Fe—N—C samples: The atomically dispersed Fe embedded in *N*-doped shattered hollow shell carbon capsules (Fe—N—C) were synthesized via in situ polymerization followed by pyrolysis of SiO_2@PANI-Fe precursors. The SiO_2@PANI-Fe precursors were fabricated by polymerizing of aniline with ammonium peroxydisulfate (APS) as the oxidant in the presence of SiO_2 particles (80 wt%). In details, 1 g SiO_2 was dispersed in 50 mL 1 M HCl by sonicating. Then, 5 mL aniline monomer was introduced into the homogeneous SiO_2 suspension and named as the solution A. The solution B consists of 50 mL 1 M HCl and 0.23 g APS. The suspension slowly turning green after the solution B was dropped into solution A under ice bath. During the polymerization of aniline monomer, 10 mM $FeCl_3 \cdot 9H_2O$ was introduced into the mixed solution. After the reaction completed, the precursors of SiO_2@PANI-Fe were obtained by filtrating, washing, and drying. The SiO_2@PANI-Fe compounds were pyrolyzed at 350 °C for 2 h with a heating rate of 1 °C min^{-1} and 900 °C for 2 h with a heating rate of 5 °C min^{-1} under N_2 atmosphere, then the atmosphere was converted to NH_3 and heated for another hour. The final product of shattered three-dimensional hollow shell Fe—N—C—NH_3 was obtained after treating with HF solution. For comparison, the Fe—N—C—N_2 were synthesized without the introduction of NH_3 atmosphere during the pyrolysis process.

2.2. Electrochemical characterization

To prepare the catalyst ink, 5 mg of the catalyst were dispersed in a mixture of 490 μL ethanol, 500 μL H_2O and 10 μL 5% Nafion by sonication for 30 min. Then, the ink was dropped onto a rotating disk electrode (RDE) or a rotating ring-disk electrode (RRDE) with a glassy carbon disk (4.0 mm diameter). The catalyst loading was about 0.4 mg cm^{-2}. The electrochemical measurements were investigated by using a CHI 760E electrochemical workstation (Chenhua, Shanghai) with a three-electrode system at room temperature. 0.1 M KOH, 0.1 M PBS (pH = 7.4) or 0.5 M H_2SO_4 aqueous solution saturated with N_2/O_2 was used as the electrolyte, a Pt foil and an Ag/AgCl electrode were employed as the counter and the reference electrode, respectively. All potentials measured were converted to the potential versus reversible hydrogen electrode (RHE) according to the equation $E_{RHE} = E_{Ag/AgCl} + 0.0592 \times pH + 0.205$ V. More details were shown in supporting information.

2.3. Materials characterization

The crystal structure was characterized by X-ray diffraction (XRD, D/MAX2500V+/PC with Cu Kα as the irradiation source). The X-ray photoelectron spectroscopy (XPS, ESCALAB250Xi with an Mg Kα achromatic X-ray source) was used to analyze the surface chemical states. The morphology was obtained by scanning electron microscope (SEM, JSM-6700F) and transmission electron microscope (TEM, JEM-2100F). The Raman spectrum was obtained by a Raman spectrometer (Renishaw InVia-plus) equipped with 633 nm excitation lasers. N_2 adsorption measurements were performed in an ASAP 2020 Micromeritics apparatus. The scanning transmission electron microscopy (STEM) was investigated in real time using a Titan Themis transmission electron microscopy equipped with CEOS probe and image aberration corrector operated at 200 KV.

3. Results and discussion

The geometrically optimized three-dimensional hierarchical architectures single atomic Fe—N—C catalyst were prepared via

in situ polymerization of aniline monomer on the surface of SiO_2 templates followed by the pyrolysis under N_2 and NH_3 atmosphere (Fig. 1). To obtain the unique thin carbon shell, the monodispersed SiO_2 nanospheres were employed as the template. During the evenly coating of polyaniline (PANI) on the surface of the SiO_2 spheres by APS, a moderate amount of $FeCl_3 \cdot 9H_2O$ was introduced into the reaction system. The Fe^{3+} were adsorbed and trapped into the PANI layer, resulting in the formation of atomically dispersed Fe anchored on the PANI shells (SiO_2@PANI-Fe). After pyrolyzing under an inert N_2 and NH_3 atmosphere, the coated PANI-Fe layers were carbonized into N-doped carbon and formed the active sites of Fe-N_x. Finally, the shattered hollow shelled Fe—N—C catalysts were obtained by removing the SiO_2 templates by HF solution etching.

The as-prepared structure optimized Fe—N—C catalyst hold three-dimensional hierarchical architectures. As shown in Fig. 2c and Fig. S1c, d, the morphology of Fe—N—C—NH_3 shows a broken "ball skin" structure, consistent with the size of SiO_2 spheres with a uniform diameter of 200 ± 50 nm (Fig. 2a, Fig. S1a, b). The shell thickness of the sphere is about 20 nm, which is similar to the general 2D structured materials, facilitating the mass transfer during ORR progress [26]. Macroscopically, the shells of these hollow nanospheres are staggered and overlapped to form a 3D frame structure, which is expected to improve the long-range transport of electrons in the Fe—N—C composite and ameliorate the kinetic of ORR [27]. The morphology of Fe—N—C—N_2 (Fig. S1e, f) was almost the same with Fe—N—C—NH_3. In addition, the FTIR spectra of SiO_2@PANI in Fig. 2b was measured and the spectra of PANI matches well with the previously reported work [28]. The stretching vibration of the quinine ring at 1576 cm^{-1} and of the benzene ring at 1495 cm^{-1} as well as the C—N stretching vibration of the secondary aromatic amine at 1302 cm^{-1} were observed. The peak at 1248 cm^{-1} commonly ascribed to the C—$N^{+\bullet}$ stretching vibration in the polaron structure was also viewed, successfully confirming the presence of PANI layer in the doped state [29,30].

This unique and well-defined structure can be attributed to a variety of factors: (i) The silicon hydroxyl group forms a moderate chemical bond (hydrogen bonding) with the hydrogen atom on the –NH group of the aniline molecule, which makes the aniline molecule monolayer adsorbed on the silicon sphere surface. With the monolayer aniline as a nucleation center, anilines were initiated to polymerize in the later stage to obtain a uniformly coated and adjustable thickness polyaniline on the surface; (ii) Based on the hard and soft acids and bases theory, Fe^{3+} ion is a hard acid and tends to bind with the amine group. The –NH group in the polyaniline molecule complexed with iron ions and evenly dispersed/anchored in the conductive network structure of PANI, enhancing the formation of single atomic active centers; (iii) the introduction of NH_3 during the pyrolysis process helps to repair the defects of pyridine nitrogen and forms more uniform Fe-N_x active centers; (iv) the introduction of NH_3 plays a vitally role in activating the graphitized carbon skeleton and increase the number of active sites. At the same time, the 3D thin-walled layered porous structure can fully "breathe" and allow oxygen to enter the catalyst and participate in the ORR process, thus improve the long-range fast-transportation ability of electrons. This is more conducive to the kinetics of the ORR process [31].

The atomically dispersed Fe—N—C sample was developed by post-molecule pyrolysis assisted with silicon template and reconstructed by ammonia treatment. As shown in the X-ray diffraction (XRD) patterns (Fig. 3a), only two broad peaks appear at 2θ of around 25° and 44°, which belong to (002) and (100) diffractions of carbon matrix [32]. No visible diffraction peak owing to Fe or Fe compounds were observed, indicating that the acid treatment removed the Fe particles or Fe element might exist in the modality of isolated single atoms. This result also be detected in transmission electron microscopy (TEM) images (Fig. 3b and c), further demonstrated that Fe atoms might uniformly scattered on the carbon network. To confirm the speciation of Fe element, the high-angle annular dark-field scanning transmission electron microscopy (HAADF-STEM) was adopted. As shown in Fig. 3d, the Fe—N—C—NH_3 composite also shows a shattered spherical morphology, corresponding to the results of SEM and TEM images. In addition, the electron energy-loss spectroscopy (EELS) verified the Fe, N, and C elements are uniformly distributed on the carbon skeleton (Fig. 3e). Moreover, the well-dispersed bright dots marked with yellow cycles represented isolated Fe atoms (Fig. 3f).

The graphite carbon appeared in the XRD patterns were further affirmed by Raman spectra. As shown in Fig. 4a, both the Fe—N—C—NH_3 and Fe—N—C—N_2 exhibit typical D band and G band of carbon at about 1335 cm^{-1} and 1596 cm^{-1}, respectively[33]. G band is related to the graphitic carbon while D band attributes to the disordered/defected carbon structures. The ratio of D and G bands (I_D/I_G) is usually used to indicate the degree of carbon defects. In Fig. 4a, the I_D/I_G of Fe—N—C—NH_3 is 1.35, larger than Fe—N—C—N_2 (1.07), suggesting that NH_3 treatment is contribute to the formation of the disordered/defective carbon, which was deemed as the crucial composite for the adsorption of O_2 during ORR process [34]. Furthermore, NH_3 treatment also helps to increase the specific surface area of the Fe—N—C composites. As shown in Brunauer-Emmet-Teller (BET) adsorption/desorption isotherm (Fig. 4b), both the Fe—N—C—NH_3 and Fe—N—C—N_2 have a duplicate typical IV isotherm curve which illustrate a homologous porous structure. Besides, the remarkable hysteresis loops of the resultant catalysts in BET consequences indicated their mesoporous nature due to the decomposition of PANI and NH_3 activa-
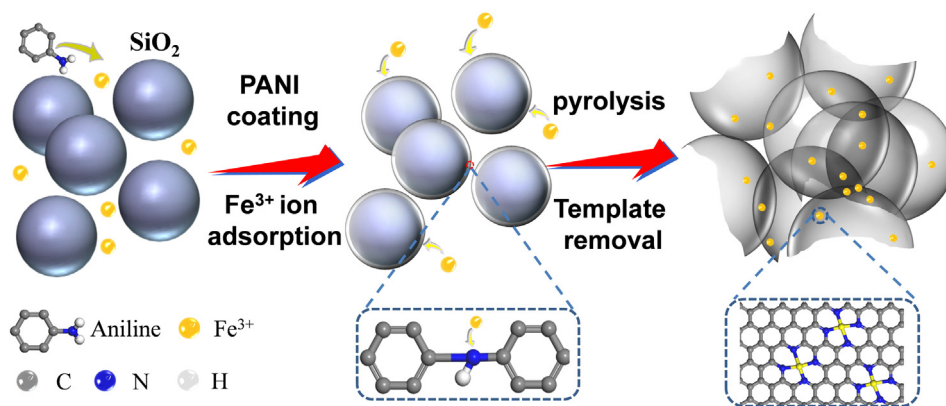

Fig. 1. A schematic illustration of the synthetic process of the atomically dispersed 3D Fe—N—C—NH_3 electrocatalyst.
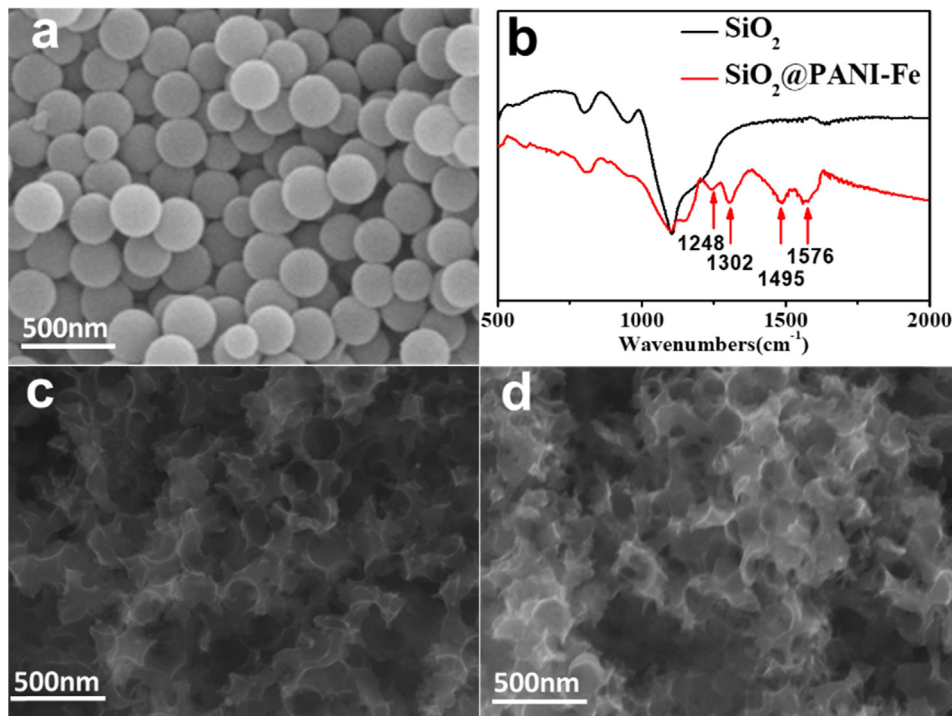
Fig. 2. (a) SEM image of SiO₂ templates; (b) FTIR spectrum of SiO₂ and SiO₂@PANI-Fe; (c) SEM image of Fe—N—C—NH₃; (d) SEM image of Fe—N—C—N₂.
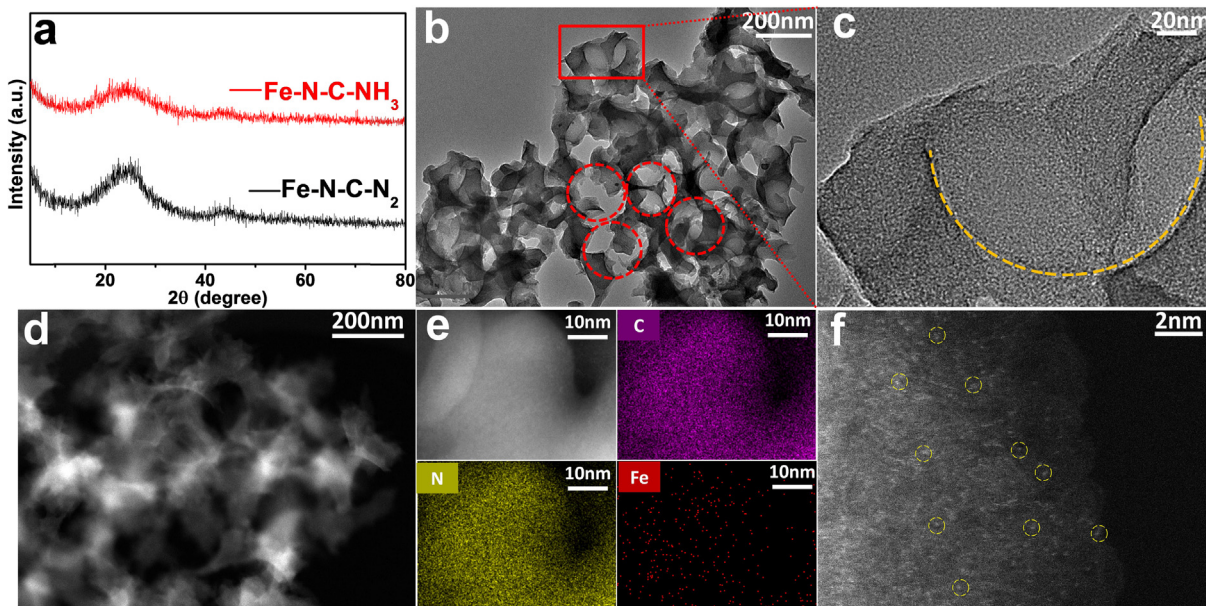

Fig. 3. (a) XRD patterns of Fe—N—C—N₂ and Fe—N—C—NH₃ sample; (b, c) TEM images of Fe—N—C—NH₃; (d) Magnified HAADF-STEM image of Fe—N—C—NH₃; (e) EFTEM elemental mapping of Fe—N—C—NH₃; (f) HAADF-STEM image of Fe—N—C—NH₃. Some single Fe atoms are highlighted by yellow circles.

tion. The BET surface areas of Fe—N—C—NH₃ (436.7 m² g⁻¹) is almost 2 times of Fe—N—C—N₂ (225.3 m² g⁻¹) sample, significantly demonstrating that secondary pyrolysis was essential to boost the surface area for *N*-doped carbon materials. In addition, the distribution of micropores and mesopores in Fe—N—C—NH₃ is exhibited in Fig. S2.

To further explore the electronic structure and surface composition of Fe—N—C—NH₃, the X-ray photoelectron spectroscopy (XPS) was performed. In Fig. 4d, the high-resolution Fe 2p spectrum reveals two peaks for Fe³⁺ 2*p* 1/2 (714.2 eV) and Fe²⁺ 2*p*

3/2 (725.5 eV) [35,36]. Additionally, the peak lies in 711.3 eV can be distributed to Fe-N$_x$ species, demonstrating the formation of Fe-N configuration [10,37]. The N 1s spectrum of the Fe—N—C—NH₃ can be deconvoluted into four peaks at 403.2, 400.8, 399.6, and 398.2 eV, corresponding to oxidized-N, graphitic-N, pyrrolic-N, and pyridinic N (or Fe-N), respectively (Fig. 4e). It is well-known that the pyridinic-N plays a crucial role in the formation of M-N$_x$ active sites with modified local electronic structure and the graphitic-N are favorable for the transportation of intermediate substances during ORR progress [32,38]. However,

it has also been speculated that graphitic-N has the catalytic activity of ORR, and the specific mechanism has not been confirmed. The content of graphitized nitrogen in Fe—N—C—NH₃ is less than that of in Fe—N—C—N₂. Interestingly, the pyridinic-N (49.6%) content of Fe—N—C—NH₃ significantly increased compared with Fe—N—C—N₂ (30.0%) according to the XPS results (Fig. S3 and Table S1), demonstrating that NH₃ treating is vital to the formation of pyridinic-N. The C 1s spectrum of Fe—N—C—NH₃ (Fig. 4f) shows four distinct peaks at 284.6, 285.7, 287.4 and 289.1 eV, corresponding to C—C, C—N, C—O and C=O, respectively. The C—N concentration in the composites also shows different, and C—N group in Fe—N—C—NH₃ is more than that of synthesized in N₂, confirming that NH₃ treatment can reconstruct the Fe-N₄ active sites and more active sites are obtained. Similarly, C—O and C=O groups content in Fe—N—C—NH₃ is scarce (Table S1), indicating the improved electron conductivity, which is helpful to relieve electrochemical polarization caused by electron transfer [39]. In addition, the Fe contents of Fe—N—C—N₂ and Fe—N—C—NH₃ were quantified to be 4.77 wt% and 7.07 wt% by the inductively coupled plasma mass spectrometry (ICP-MS) (Table S3). The Fe—N—C—NH₃ composite containing single atomic active sites with more pyridinic-N would be profitable for ORR in full pH electrolytes.

We utilized a systemic strategy to synthesize an atomically dispersed Fe scattered on shattered hollow shell *N*-doped carbon substrate catalyst. To understand the reaction behavior and durable ability of this sample under different pH electrolytes, we explored the ORR performance of these catalysts in alkaline (0.1 M KOH), neutral (0.1 M PBS, pH = 7.4), and acid (0.5 M H₂SO₄) mediums, respectively.

Firstly, the ORR activity of this well-designed Fe—N—C catalyst was estimated in 0.1 M KOH electrolyte with RDE technique. As shown in Fig. S4, the CV curves of the Fe—N—C—NH₃ shows a typical rectangle-like shape in N₂-saturated electrolytes, and the current contribution is attributed to the capacity of *N*-doped carbon. While a well-defined oxygen reduction peak at around 0.8 V appeared in O₂-saturated KOH solution, suggesting a considerable ORR activity for Fe—N—C—NH₃. The ORR electrocatalytic activity was further investigated by the linear sweep voltammograms (LSVs) measurements (Fig. 5a). The Fe—N—C—NH₃ shows an onset potential (E_{onset}) of 0.98 V and a half-wave potential ($E_{1/2}$) of 0.85 V,

as well as a limiting current density (J_L) of around 5.1 mA cm^{-2}. Compared with Fe—N—C—N₂, the catalytic activity ($E_{1/2}$, E_{onset}, and J_L) of atomically dispersed Fe—N—C—NH₃ got a significant improvement when treated with NH₃. Moreover, the performance of the Fe—N—C—NH₃ even comparable to the state-of-the-art Pt/C and beyond most of the previously reported single atom ORR electrocatalysts (Table S2). Consequently, further proved that pyridinic-N coordinated with iron species is essential for ORR activity combined with the XPS results [40–42]. In Fig. 5b, we measured the LSV curves at different rotation rates from 400 to 2025 rpm and calculated the corresponding linear Koutecky-Levich (K-L) plots (Fig. 5b insert). Noteworthily, the K-L plots exhibit superior linearity at different potentials and the electron transfer number (n) was calculated to be about 4, suggesting an efficient 4e-ORR pathway on Fe—N—C—NH₃. This result was also confirmed from the rotating ring-disk electrode (RRDE) measurements in Fig. 5c, the H₂O₂ yield of Fe—N—C—NH₃ (<5%) measured by the ring current from 0.1 to 0.8 V, lower than that of Fe—N—C—N₂ (~15%) and commercial Pt/C (~8.5%). This further confirmed a direct four-electron pathway and an excellent catalytic activity for Fe—N—C—NH₃.

In Fig. 5d, the Fe—N—C—NH₃ shows the lowest Tafel slope of 85 mV dec^{-1} compared with the Fe—N—C—N₂ (114 mV dec^{-1}) and Pt/C (94 mV dec^{-1}), suggesting it's outstanding kinetic for ORR beyond Pt/C. Moreover, the methanol tolerance test is also particularly important, considering the application of this atomically dispersed Fe—N—C catalyst in direct methanol fuel cells (DEMFC). As shown in Fig. 5e, the current density of Pt/C shows a dramatical loss after the introduction of 2 M methanol. While there is no appreciable variation for Fe—N—C—NH₃, indicating its outstanding tolerance to methanol poisoning. In addition, the chronoamperometric responses were performed to evaluate the durability of Fe—N—C—NH₃. In Fig. 5f, the Fe—N—C—NH₃ exhibits a superior stability with a slightly current attenuation of 2.5% in 30000 s, whereas the Pt/C suffers a rapid loss of 26.5% in 10000 s. The above results further confirm the unparalleled ORR activity of Fe—N—C—NH₃ in alkaline electrolyte.

We continued to investigate its catalytic activity in acid and neutral medium, respectively. A broad ORR peak at about 0.5 V is visible in Fig. 6a, suggesting the positive ORR activity for
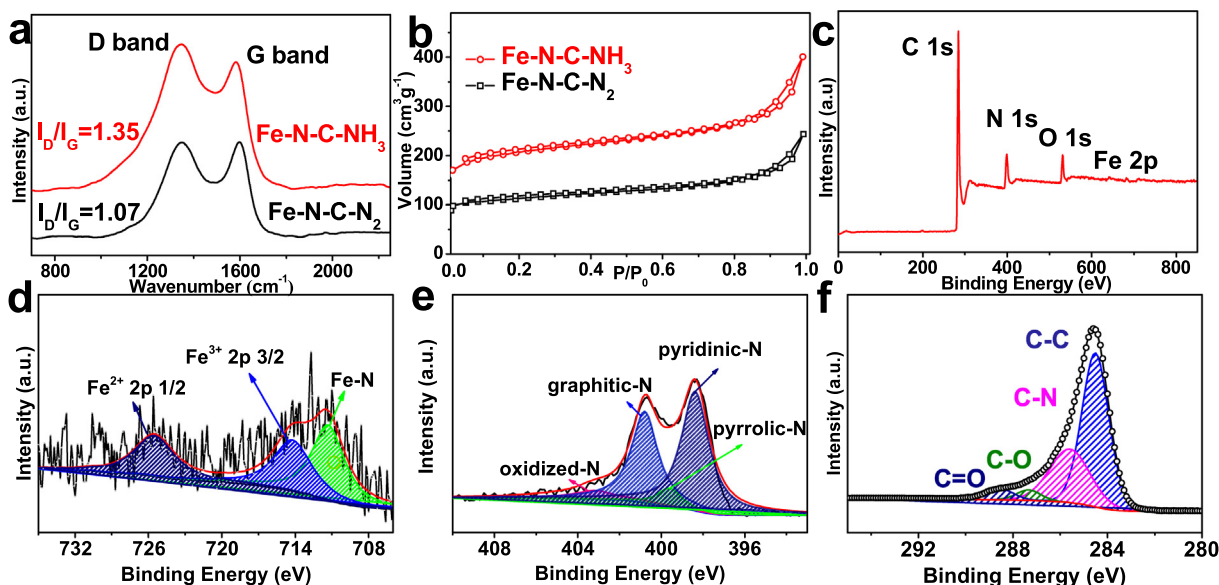

Fig. 4. (a) Raman spectra of Fe—N—C—N₂ and Fe—N—C—NH₃; (b) N₂ isothermal adsorption/desorption curves of Fe—N—C—N₂ and Fe—N—C—NH₃; (c) XPS spectrum of Fe—N—C—NH₃; High-resolution XPS spectra of (d) Fe 2p, (e) N 1s, (f) C 1s.
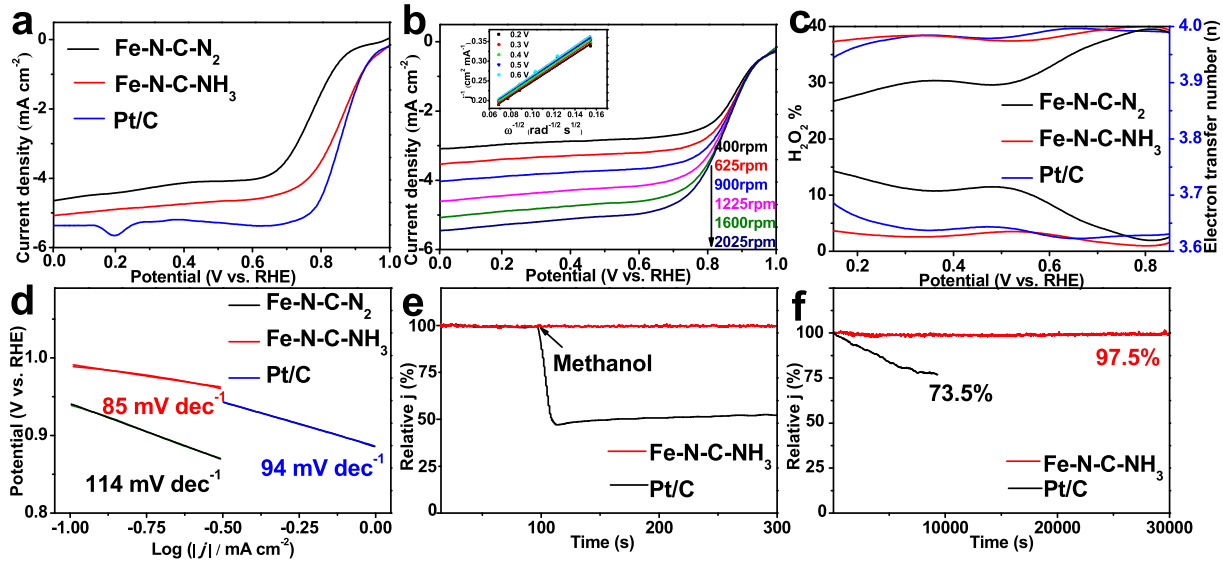
Fig. 5. (a) LSV curves of Fe—N—C—N_2, Fe—N—C—NH_3, and commercial Pt/C in 0.1 M KOH solution; (b) LSV curves of Fe—N—C—NH_3 at different rotation speeds (400–2025 rpm), inset is the corresponding K-L plots; (c) H_2O_2 yield and transferred electron of Fe—N—C—N_2, Fe—N—C—NH_3, and Pt/C; (d) Tafel plots of Fe—N—C—N_2, Fe—N—C—NH_3, and Pt/C; (e) Methanol tolerance of Fe—N—C—NH_3 and Pt/C; (f) I-t curves of Fe—N—C—NH_3 and Pt/C at 0.7 V.

Fe—N—C—NH_3 in acid medium. The LSV curves (Fig. 6b) reveal an outstanding activity for Fe—N—C—NH_3 ($E_{1/2}$ = 0.65 V, E_{onset} = 0.92 V, J_L = 4.5 mA cm^{-2}) compared with the Fe—N—C—N_2 ($E_{1/2}$ = 0.33 V, E_{onset} = 0.57 V, J_L = 3.4 mA cm^{-2}). Besides, the Fe—N—C—NH_3 possesses the fast ORR kinetics compared with the Pt/C and Fe—N—C—N_2 samples in Figure S5a. Moreover, the Fe—N—C—NH_3 also exhibits excellent tolerance to methanol and long-time stability in acid electrolyte (Fig. S5b, S5c). All above results further confirm that the NH_3 treatment plays a vital role in boosting the ORR performance by reconstructing Fe-N_4 active sites. In addition, the RRDE tests (Fig. 6c) also show that the H_2O_2 yield on the Fe—N—C—NH_3 catalyst is below 5%, a bit lower than the commercial Pt/C but obviously superior to Fe—N—C—N_2 (above 10%).

In Fig. 6d, the CV curve of Fe—N—C—NH_3 represents a sharp reduced peak at about 0.55 V, similar to the cases in 0.1 M KOH and 0.5 M H_2SO_4. In neutral solution, the Fe—N—C—NH_3 also
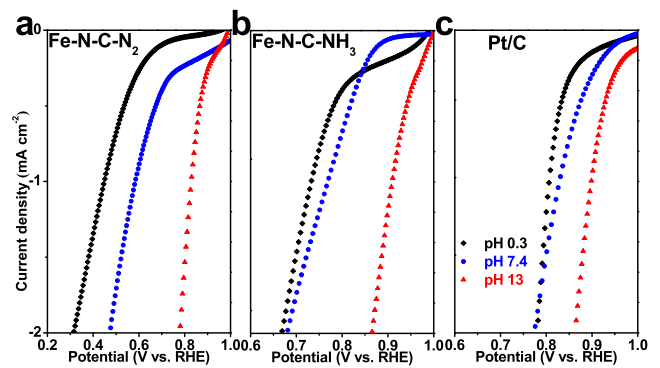

Fig. 7. LSV profiles of (a) Fe—N—C—N_2, (b) Fe—N—C—NH_3 and (c) Pt/C at different pH values.
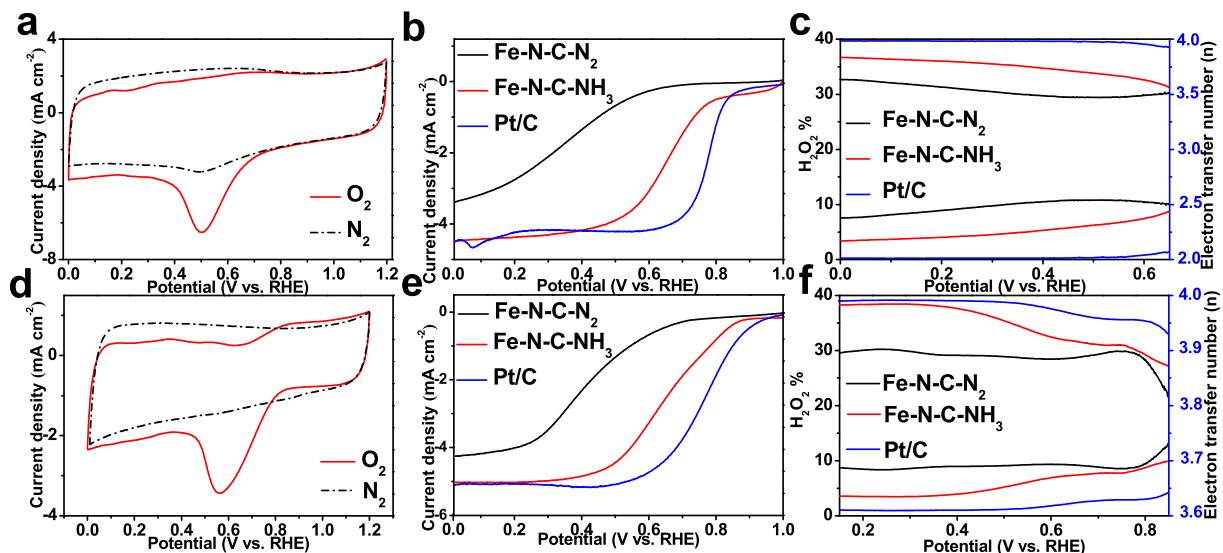
Fig. 6. CV curves of Fe—N—C—NH_3 in N_2– and O_2-saturated (a) 0.5 M H_2SO_4 solution, (d) 0.1 M PBS solution. LSV curves of Fe—N—C—NH_3, Fe—N—C—N_2, and Pt/C in (b) 0.5 M H_2SO_4 solution, (e) 0.1 M PBS solution·H_2O_2 yield and transferred electron of Fe—N—C—NH_3, Fe—N—C—N_2, and Pt/C in (c) 0.5 M H_2SO_4 solution, (f) 0.1 M PBS solution.

exhibits a superior ORR performance ($E_{1/2}$ = 0.65 V, E_{onset} = 0.86 V, J_L = 5.0 mA cm^{-2}), significantly superior to that of the Fe—N—C—N$_2$ (Fig. 6e). Although the $E_{1/2}$ of Fe—N—C—NH$_3$ cannot be compared with the start-of-the-art commercial Pt/C ($E_{1/2}$ = 0.77 V), the E_{onset} and J_L are very similar to the Pt/C. Besides, the RRDE test (Fig. 6f) reveals that the H$_2$O$_2$ yield on the Fe—N—C—NH$_3$ cathode is below 4%, compared to that of Pt/C (below 2.5%), but obviously superior to that of the Fe—N—C—N$_2$ (above 9%). The lowest Tafel slope of Fe—N—C—NH$_3$ also means the fast kinetics for ORR (Figure S6a). Moreover, the Fe—N—C—NH$_3$ exhibits superior long-time stability and extraordinary tolerance to methanol in neutral electrolyte in Figure S6b and Figure S6c.

Interestingly, we find a meaningful phenomenon that there is a significant difference of the n values in different pH values. In general, the n values of Fe—N—C—NH$_3$ in 0.1 M KOH electrolyte are larger than that of in 0.5 M H$_2$SO$_4$ and 0.1 M PBS. This indicates that there are various reaction mechanisms due to the different concentrations of H$^+$ and OH$^-$ and different rate-determining steps. Furthermore, combining the H$_2$O$_2$ yield of Fe—N—C—NH$_3$ and Fe—N—C—N$_2$, we discovered that the Fe—N—C—N$_2$ always possesses a high H$_2$O$_2$ yield, especially in acid medium (above 10%). This indicates that there is a mixed reaction including 2e-ORR and 4e-ORR of Fe—N—C—N$_2$ during ORR progress. To investigate the origin of the 2e-ORR, we detected the oxygen-containing groups in XPS results in Fig. 4 and Table S1, which were deem as the active sites of the production of hydrogen peroxide. Based on that, a coupled proton-electron transfers (CPETs) mechanism was reported, in which a combined 2e- or 4e-ORR mechanism was attributed to the content of oxygen-containing groups and the sp^2 C [43]. In Fig. 4, the oxygen contents of the as-synthesized Fe—N—C decreased noticeably after NH$_3$ treatment. That is why the Fe—N—C—NH$_3$ possesses a superior selectivity during ORR progress. In addition, the content of pyridinic-N increased when NH$_3$ attacked the unsaturated bond of the defect edge of carbon matrix, and this result is corresponding to XPS spectrum and electrochemical tests. In Table S1, the Fe—N—C—NH$_3$ remains dominant contents of pyridinic-N compared with the Fe—N—C—N$_2$. This confirms that NH$_3$ treatment can evidently improve the number of Fe-N$_4$ active sites and reconstruct the types of active sites [44], thereby greatly enhancing the ORR catalytic activity. Moreover, the content of oxygen species reduced from 14.67% to 5.54% after secondary pyrolysis with ammonia, thus reducing the generation of hydrogen peroxide.

Generally, the CPETs is the process of protonation and electron transfer at the same time. The energy barriers required by the ORR progress will decrease and the reaction is convenient to proceed if this process can be easily carried out, thus requires quality conductivity and sufficient active sites for catalysts. As for the Fe—N—C—N$_2$ and the Fe—N—C—NH$_3$, pyrolyzing with the same temperature, the conductivity cannot be the dominant reason that contribute to the CPETs mechanism. Therefore, the only influencing factor for our catalysts is the active sites. The contained Fe and pyridinic-N components in the Fe—N—C—NH$_3$ which constitute the Fe-N$_4$ active sites are obviously higher than that of the Fe—N—C—N$_2$ according to the XPS results (Table S1). As a result, the Fe—N—C—NH$_3$ electrocatalyst occupies relatively 4e-ORR selectivity and superior stability in full pH electrolyte. Under the current density of 2 mA cm^{-2}, the narrow onset potential range (from 0.65 V to 0.85 V) shows that the Fe—N—C—NH$_3$ mainly possesses a CPETs mechanism (Fig. 7b). For Fe—N—C—N$_2$, the pH dependence is relatively strong owing to the inferior active sites (Fig. 7a), which indicates the Fe—N—C—N$_2$ exhibits a mixed 2e-ORR and 4e-ORR process and possess a typical non-CPETs control process. Moreover, the Pt/C follows a 4e-ORR process and a CPETs mechanism similar to the Fe—N—C—NH$_3$ in Fig. 7c.

4. Conclusion

In summary, we successfully construct a structural optimized hollow shattered spherical atomically dispersed Fe—N—C catalyst assisted with silica template and secondary pyrolysis method. The secondary pyrolysis with ammonia atmosphere reconstructs the nitrogen types and significantly enhances the contents of Fe-N$_x$ active sites. This three-dimensional structure with a great quantity of mesoporous are conducive to the transportation of protons and electrons during ORR progress. STEM results demonstrate the existence of Fe single atoms with Fe-N$_4$ configuration and XPS measurements reveal the different functions of the distinct N species. Benefiting from the novel structure and unique coordination environment, the as-prepared Fe—N—C catalyst delivers outstanding ORR catalytic activity, excellent stability, as well as distinguished tolerance to methanol poisoning in pH-universal electrolyte, compared to that of Pt/C and most reported state-of-the-art single atom catalysts, showing a promising application in PEMFCs and metal-air batteries.

CRediT authorship contribution statement

Zhe Chen: Conceptualization, Formal analysis. **Dengyu Zhao:** Methodology, Investigation, Formal analysis. **Cong Chen:** Data curation. **Yuan Xu:** Formal analysis. **Congli Sun:** Methodology. **Kangning Zhao:** . **Muhammad Arif Khan:** Validation. **Daixin Ye:** Validation, Funding acquisition. **Hongbin Zhao:** Supervision, Funding acquisition. **Jianhui Fang:** Project administration. **Xueliang Andy Sun:** Project administration. **Jiujun Zhang:** Project administration.

Declaration of Competing Interest

The authors declare that they have no known competing financial interests or personal relationships that could have appeared to influence the work reported in this paper.

Acknowledgement

Appendix A. Supplementary data

Supplementary data to this article can be found online at https://doi.org/10.1016/j.jcis.2020.08.103.

References

[1] J. Li, M. Chen, D.A. Cullen, S. Hwang, M. Wang, B. Li, K. Liu, S. Karakalos, M. Lucero, H. Zhang, C. Lei, H. Xu, G.E. Sterbinsky, Z. Feng, D. Su, K.L. More, G. Wang, Z. Wang, G. Wu, Nat. Catal. 1 (2018) 935–945.
[2] I.S. Amiinu, Z. Pu, X. Liu, K.A. Owusu, H.G.R. Monestel, F.O. Boakye, H. Zhang, S. Mu, Adv. Funct. Mater. 27 (2017) 1702300.
[3] W. Cao, Y. Xu, Z. Wang, J. Luo, M.A. Khan, L. Zhang, D. Ye, H. Zhao, J. Zhang, J. Electrochem. Soc. 167 (2020) 104511.
[4] J.X. Wu, W.W. Yuan, M. Xu, Z.Y. Gu, Chem. Commun. 55 (2019) 11634–11637.
[5] L. Cao, Z. Zhao, Z. Liu, W. Gao, S. Dai, J. Gha, W. Xue, H. Sun, X. Duan, X. Pan, T. Mueller, Y. Huang, Matter 1 (2019) 1567–1580.
[6] Y. Han, Y.G. Wang, W. Chen, R. Xu, L. Zheng, J. Zhang, J. Luo, R.A. Shen, Y. Zhu, W.C. Cheong, C. Chen, Q. Peng, D. Wang, Y. Li, J. Am. Chem. Soc. 139 (2017) 17269–17272.
[7] J.X. Wu, S.Z. Hou, X.D. Zhang, M. Xu, H.F. Yang, P.S. Cao, Z.Y. Gu, Chem. Sci. 10 (2019) 2199–2205.
[8] D. Ji, L. Fan, L. Tao, Y. Sun, M. Li, G. Yang, T.Q. Tran, S. Ramakrishna, S. Guo, Angew. Chem. Int. Ed. Engl. 58 (2019) 13840–13844.
[9] C. Du, P. Li, F. Yang, G. Cheng, S. Chen, W. Luo, A.C.S. Appl. Mater. Interfaces 10 (2018) 753–761.
[10] Z. Huang, H. Pan, W. Yang, H. Zhou, N. Gao, C. Fu, S. Li, H. Li, Y. Kuang, ACS Nano 12 (2018) 208–216.

[11] G.A. Ferrero, K. Preuss, A. Marinovic, A.B. Jorge, N. Mansor, D.J. Brett, A.B. Fuertes, M. Sevilla, M.M. Titirici, ACS Nano 10 (2016) 5922–5932.
[12] H. Ren, Y. Wang, Y. Yang, X. Tang, Y. Peng, H. Peng, L. Xiao, J. Lu, H.D. Abruña, L. Zhuang, ACS Catal. 7 (2017) 6485–6492.
[13] P. Chen, T. Zhou, L. Xing, K. Xu, Y. Tong, H. Xie, L. Zhang, W. Yan, W. Chu, C. Wu, Y. Xie, Angew. Chem. Int. Ed. Engl. 56 (2017) 610–614.
[14] Y. He, S. Hwang, D.A. Cullen, M.A. Uddin, L. Langhorst, B. Li, S. Karakalos, A.J. Kropf, E.C. Wegener, J. Sokolowski, M. Chen, D. Myers, D. Su, K.L. More, G. Wang, S. Litster, G. Wu, Energy Environ. Sci. 12 (2019) 250–260.
[15] L. Zhang, Y. Jia, G. Gao, X. Yan, N. Chen, J. Chen, M.T. Soo, B. Wood, D. Yang, A. Du, X. Yao, Chem 4 (2018) 285–297.
[16] J. Gu, C.-S. Hsu, L. Bai, H.M. Chen, X. Hu, Science 364 (2019) 1091–1094.
[17] J. Li, S. Chen, F. Quan, G. Zhan, F. Jia, Z. Ai, L. Zhang, Chem 6 (2020) 885–901.
[18] Y. Chen, Z. Li, Y. Zhu, D. Sun, X. Liu, L. Xu, Y. Tang, Adv. Mater. 31 (2019) e1806312.
[19] X. Wang, Y. Jia, X. Mao, D. Liu, W. He, J. Li, J. Liu, X. Yan, J. Chen, L. Song, A. Du, X. Yao, Adv. Mater. (2020) e2000966.
[20] X. Yan, Y. Jia, K. Wang, Z. Jin, C.L. Dong, Y.C. Huang, J. Chen, X. Yao, Carbon Energy 2020 (2020) 1–9.
[21] F. Liu, G. Zhu, D. Yang, D. Jia, F. Jin, W. Wang, RSC Adv. 9 (2019) 22656–22667.
[22] J. Yang, X. Wang, B. Li, L. Ma, L. Shi, Y. Xiong, H. Xu, Adv. Funct. Mater. 27 (2017) 1606497.
[23] X. Wang, Z. Li, Y. Qu, T. Yuan, W. Wang, Y. Wu, Y. Li, Chem 5 (2019) 1486–1511.
[24] H. Shen, E. Gracia-Espino, J. Ma, K. Zang, J. Luo, L. Wang, S. Gao, X. Mamat, G. Hu, T. Wagberg, S. Guo, Angew. Chem. Int. Ed. Engl. 56 (2017) 13800–13804.
[25] X. Fu, N. Li, B. Ren, G. Jiang, Y. Liu, F.M. Hassan, D. Su, J. Zhu, L. Yang, Z. Bai, Z.P. Cano, A. Yu, Z. Chen, Adv. Energy Mater. 9 (2019) 1803737.
[26] D. Li, C. Lv, L. Liu, Y. Xia, X. She, S. Guo, D. Yang, A.C.S. Cent, Sci. 1 (2015) 261–269.
[27] Y. Chen, S. Ji, S. Zhao, W. Chen, J. Dong, W.C. Cheong, R. Shen, X. Wen, L. Zheng, A.I. Rykov, S. Cai, H. Tang, Z. Zhuang, C. Chen, Q. Peng, D. Wang, Y. Li, Nat. Commun. 9 (2018) 5422.
[28] L. Zhang, L. Liang, W. Su, S. Liu, J. Chen, Chinese J. Chem. 29 (2011) 2552–2556.
[29] M. Trchová, J. Stejskal, Pure Appl. Chem. 83 (2011) 1803–1817.
[30] B. Butoi, A. Groza, P. Dinca, A. Balan, V. Barna, Polymers (Basel) 9 (2017) 732.
[31] W. He, C. Jiang, J. Wang, L. Lu, Angew. Chem. Int. Ed. Engl 53 (2014) 9503–9507.
[32] L. Lin, Q. Zhu, A.W. Xu, J. Am. Chem. Soc. 136 (2014) 11027–11033.
[33] S. Li, C. Cheng, H.-W. Liang, X. Feng, Adv. Mater 29 (2017) 1700707.
[34] J. Zhu, W. Li, S. Li, J. Zhang, H. Zhou, C. Zhang, J. Zhang, S. Mu, Small 14 (2018) e1800563.
[35] X. Wang, H. Zhang, H. Lin, S. Gupta, C. Wang, Z. Tao, H. Fu, T. Wang, J. Zheng, G. Wu, X. Li, Nano Energy 25 (2016) 110–119.
[36] M. Xiao, J. Zhu, L. Ma, Z. Jin, J. Ge, X. Deng, Y. Hou, Q. He, J. Li, Q. Jia, S. Mukerjee, R. Yang, Z. Jiang, D. Su, C. Liu, W. Xing, ACS Catal. 8 (2018) 2824–2832.
[37] W. Zhang, X. Xu, C. Zhang, Z. Yu, Y. Zhou, Y. Tang, P. Wu, S. Guo, Small Methods 1 (2017) 1700167.
[38] F. Tang, H. Lei, S. Wang, H. Wang, Z. Jin, Nanoscale 9 (2017) 17364–17370.
[39] I.S. Amiinu, X. Liu, Z. Pu, W. Li, H. Tang, S. Mu, Adv. Funct. Mater. 1704638 (2017).
[40] M. Primbs, Y. Sun, A. Roy, D. Malko, A. Mehmood, M.-T. Sougrati, P.-Y. Blanchard, G. Granozzi, T. Kosmala, G. Daniel, P. Atanassov, J. Sharman, C. Durante, A. Kucernak, D. Jones, F. Jaouen, P. Strasser, Energy Environ. Sci. (2020), https://doi.org/10.1039/d0ee01013h.
[41] L. Gong, H. Zhang, Y. Wang, E. Luo, K. Li, L. Gao, Y. Wang, Z. Wu, Z. Jin, J. Ge, Z. Jiang, C. Liu, W. Xing, Angew. Chem. Int. Ed. Engl. 132 (2020) 2–8.
[42] B. Li, S.P. Sasikala, D.H. Kim, J. Bak, I.-D. Kim, E. Cho, S.O. Kim, Nano Energy 56 (2019) 524–530.
[43] H.W. Kim, V.J. Bukas, H. Park, S. Park, K.M. Diederichsen, J. Lim, Y.H. Cho, J. Kim, W. Kim, T.H. Han, J. Voss, A.C. Luntz, B.D. McCloskey, ACS Catal. 10 (2020) 852–863.
[44] Y. Wang, H. Liu, K. Wang, S. Song, P. Tsiakaras, Appl. Catal. B Environ. 210 (2017) 57–66.